Design study of a low emittance complex bend achromat lattice

Minghao Song* and Timur Shaftan
Brookhaven National Laboratory, Upton, New York 11973, USA

(Received 4 December 2023; accepted 15 May 2024; published 11 June 2024)

Light sources worldwide have experienced rapid growth in the last decades, pushing toward higher brightness with lower emittance to meet growing demands from the user community. The quest for higher brightness motivates the development of low-emittance ring lattices. At this point, all fourth-generation storage ring light sources employ variations of the multibend achromat (MBA) lattice. In this paper, we discuss an extension of this approach, known as complex bend achromat lattice in relation to the future NSLS-II upgrade. A detailed approach for the lattice design will be described and the developed lattice will be presented. The advantages of using our complex bend approach are evident in reaching a natural emittance as low as 23 pm at a beam energy of 3 GeV, providing a straight section of 8.4 m for long insertion devices, and acquiring a ratio of about 50% of free space with respect to the ring circumference. The design includes the use of permanent magnets largely reducing the need for power supplies. Our new approach provides an extension to the MBA concept for the next-generation light source lattice design.

DOI: 10.1103/PhysRevAccelBeams.27.061601

I. INTRODUCTION

Through the past few decades, synchrotron radiation light sources have become major hubs for modern applied science and have been driving research in various fields ranging from biology to physics, chemistry, and material science. Modern synchrotron light source accelerator technology continues to expand its capabilities to produce bright and coherent radiation targeting the diffraction-limit for high energy x-ray beams.

The brightness of synchrotron radiation is one of the key characteristics of the source. It is defined by the electron beam emittance and intensity in combination with the chosen insertion device and the x-ray beam size and divergence in a source point. Following the quest to increase the source brightness, the ring designers seek ways to reduce the beam emittance. The electron beam emittance ϵ_{x0} defined by the storage ring lattice scales as $E^2/[N_c N_b]^3$, where E is the beam energy, N_c is the number of cells in a ring, and N_b is the number of bending magnets per cell [1]. Therefore, increasing the number of dipoles is the most effective way to reach ultralow beam emittance. This was recognized in the 90s by Einfeld *et al.* [2], and currently, every modern storage ring light source upgrade project is based on a certain variant of the multibend achromat (MBA) approach. This powerful concept has been detailed for MAX-IV [3], SIRIUS [4], ESRF-EBS [5], APS-U [6], ALS-U [7,8], HEPS [9], SOLEIL II [10,11], KOREA-4GSR [12], and DLSR [13] and customized at many other light source facilities [14–16].

As one approaches the diffraction limit for the rings within a conceivable range of circumferences (< 1 km), the challenge of the available space for the ring elements becomes apparent and dominating. As an example of the ultimate lattice design for diffraction-limited source, a lattice option of the upgrade of MAX-IV [3] features a 19-BA achromat, capable of reaching 16 pm rad in the 500-m-long ring tunnel [17]. This lattice provided a high-performance solution by reducing the beam emittance with a factor of 20 compared to the operating MAX-IV ring. However, the composition of the lattice elements left very limited space for insertion devices (IDs), vacuum components, and other equipment.

This example adequately illustrates the limit of the MBA approach in its current form. It motivates the search for new accelerator technologies and lattice solutions, which is the topic of this paper. The new accelerator methodology is presented by the concept of the complex bend element [18], a long-curved magnet containing a tight arrangement of quadrupole-dipoles built using permanent magnets (PM). The R&D on PMQ magnets is an active area of research already delivering promising results at several facilities [19–22].

Our approach described in this paper is based on the concept of complex bend (CB) [23–25]. We aim to greatly increase the number of bends in the ring by superimposing dipole and quadrupole fields in the shortest CB segments, whose parameters are limited by the possible gradient in

*msong1@bnl.gov

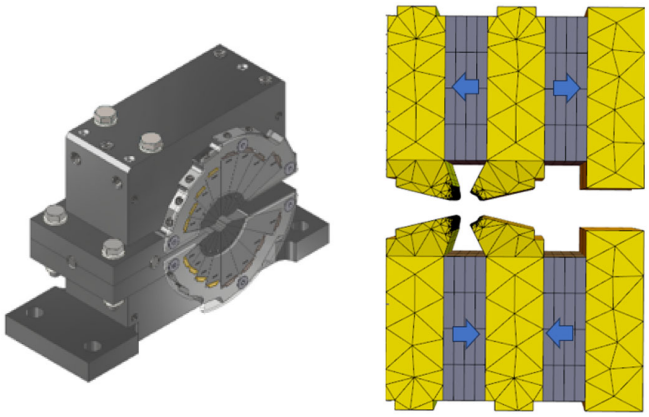

FIG. 1. Left plot: Halbach PMQ; right plot: hybrid PMQ.

PMQs at the magnet bore size constrained by the size of the extraction channel for synchrotron radiation. This leads to a modification of the expression above $\epsilon_{x0} \propto E^2/[N_c N_{CB} N_b]^3$, where N_c is the number of cells, N_{CB} is the number of complex bends per cell, and N_b is the number of short dipole-quadrupole magnets per complex bend element. To illustrate the advantage of this approach, we recall that the 7-BA APS-U lattice has a total of 280 dipoles in a ring (as compared with the APS lattice with 80 bends), while the complex bend lattice for NSLS-IIU could fit $30 \times 3 \times 30 = 900$ dipoles. This opens an opportunity to reduce the emittance further than that of MBA and achieve a compact lattice arrangement that leaves ample space for machine elements and IDs.

In the first version of a complete complex bend magnet [24], it is designed as an assembly of several complex bend single cells, with every cell providing a specific dipole field with alternating focusing and defocusing quadrupoles (QF-drift-bend-drift-QD-drift-bend-drift). In [18,24], we have shown that a much lower emittance could be reached if a regular DBA dipole is replaced by a complex bend element. Furthermore, we presented several versions of the complex bend magnet in [24,25], where the bending was achieved by either introducing an external dipole field to the pure PM quadrupole field or shifting quadrupole magnets off axis. In modeling such geometry, it has become apparent that this viable solution presents difficulties with achieving reasonable field quality at large transverse shifts of the magnets. The alternative solution that we recently developed and detailed is integrating quadrupole field into dipole field via a permanent magnet quadrupole (PMQ) of either Halbach or hybrid type [19,21], which are shown in Fig. 1. PMQ of either type will be employed in our design study of the complex bend lattice described below.

This paper complements ongoing efforts on designing the complex bend element and focuses on developing the lattice based on such elements. The optics that we describe here rely on a large number of short PMQs with the fields and strengths tailored to minimize Courant-Snyder invariant $\mathcal{H}$ [1] while adjusting Twiss functions for their optimal values in the chromatic sections, matching sections, and ID straights.

Throughout the paper, we will demonstrate the advantages of the CB approach in optimizing the following seven performance metrics in the lattice design: (i) Low emittance; (ii) long straights for IDs; (iii) sufficient space in the lattice available for accelerator equipment; (iv) perfect fitting of lattice solution to the present facility tunnel, satisfying tight constraints of overlapping ID source points with these for the existing facility beamlines; (v) minimal number of power supply for reduced power consumption; (vi) optimal beam dynamics properties for the ring lattice leading to high injection efficiency and long beam lifetime; and (vii) robustness to magnet errors and imperfections.

In this paper, we will be considering complex bend lattice for NSLS-II upgrade (NSLS-IIU) as an example. NSLS-II is a third-generation light source with a circumference of 792 m. It contains 30 DBA cells and operates at 400 mA using top-off injection [26]. The horizontal emittance is 2 nm for the bare lattice and can be reduced below 1 nm with three sets of damping wigglers. The future machine upgrade aims to increase brightness 10-fold at 1 keV to 50-fold at 10 keV of photon energy compared with the current facility.

Figure 2 shows a single cell magnet layout of the NSLS-IIU complex bend lattice candidate including multiple sections. The central CB and two outer CBs contain arrays of compact PMQ magnets. In addition, the central CB consists of left and right halves as well as the drift space between the two halves. A three-pole wiggler (3PW) is planned to be installed in the drift space of central CB, and IDs are located in the long straight and short straight, each providing the source of the photon beam.

The structure of this paper is organized as follows: Sec. II describes the approach for the complex bend lattice design. Section III discusses the design of the complex bend

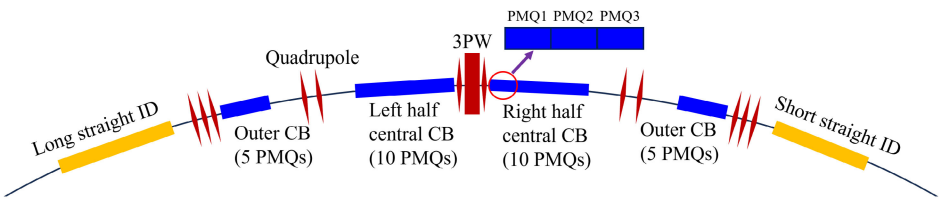

FIG. 2. Magnet layout for a single cell of NSLS-IIU complex bend lattice.

achromat (CBA) lattice for one of the developed solutions, and shows its performance compared with NSLS-II lattice and several selected MBA lattices. Section IV concludes the paper.

II. LATTICE DESIGN STRATEGY

In our approach, the search for the best lattice solution is converted into a "usual" accelerator methodology:

$$O|_{\Delta O} = \mathcal{M}|_{\Delta \mathcal{M}}(P|_{\Delta s, \Delta p}),$$

where:

(i) $P = P(s, p)$ is the vector of variables with constraints $\Delta s, \Delta p$.

(ii) O is the vector of observables with constraints ΔO. (1)

where observables in the O space include natural emittance ϵ_{x0}, natural chromaticities $\boldsymbol{\xi} = (\xi_x, \xi_y)$, radiation loss per turn U_0, momentum compaction α_c, and lengths of long and short straights $\boldsymbol{L_s} = (L_{\mathrm{LS}}, L_{\mathrm{SS}})$. $\mathcal{F} = \mathcal{F}(O, \mathrm{weight})$ is the lattice figure of merit used for selection of the best solution. ΔO are the ranges for J_x, α_c, and $\boldsymbol{L_s}$. In the P space, P variables are the strengths "s" and positions "p" of lattice elements. Δs and Δp are the allowed ranges for strengths and constraints of the magnet's positions. $\mathcal{M}$ is a functional form between O and P. In addition, there are constraints $\Delta \mathcal{M}$ related to the functional form $\mathcal{M}$. These contain geometrical limitations related to fitting to the ring tunnel and constraints imposed on the Twiss parameters.

Below, we briefly describe our approach in the lattice design [23]. The whole lattice cell is divided into a number of bins. Every one of these bins is filled with one of several lattice elements, e.g., drifts, complex bends, and quadrupoles. The strengths of the CB elements are varied within the limits given by the gradient constraints defined in the P space. The single cell is split into several sections, i.e., central complex bend, dispersion bump, outer complex bends, and straight sections. Under the P and $\mathcal{M}$ constraints, the P variables of each section are optimized to achieve the best performance in O space by using several optimization methods. The latter is based on a combination of MAD8 [27], MATLAB [28], and a suite of optimization algorithms. In the following, we describe in detail the principles of setting up the space of P, the functional form $\mathcal{M}$, the space of O, and the methods to find the optimal solution.

It is known that optimization problems fail when the number of P variables greatly exceeds the number of O observables, which is the specific challenge for the problem that we studied. Below, we describe a method that improves conditions of the P space where we use polynomial forms to reduce the dimension of P vector.

A. Setup of the P space

We start our design effort by introducing a method that we call the binning principle in the lattice layout [23]. This principle standardizes the lattice as a sequence of bins of the following five element types: drift, complex bend (CB), quadrupole, sextupole, and octupole. For instance, according to Fig. 3, a 26.4-m-long single cell of NSLS-II upgrade lattice is represented as a sequence of 264 10-cm-long bins, where adjacent bins with the same element type are grouped into an element with each type marked by a different color. It should be noted that the actual layout of elements may be adjusted based on the tunnel geometry and further design optimization.

The choice of the bin's length as 10 cm comes from the basic scale of the magnetic design of CB PMQs. According to our analysis, the lengths of permanent magnet elements PMQs will be 20 or 30 cm, producing a natural scale of focusing length within a cell.

Having digitized the lattice into 264 bins of 5 types, we can proceed to optimize the parameters of the bins, focusing on finding the optimal solutions of P variables for Eq. (1) above. Once the solution is demonstrated, we "erase" the grid and continue with the final tuning of the lattice where the locations of components are unconstrained longitudinally unless they are a part of the three complex bends.

The initial setup of bins contains three element types: drift, quadrupole, and complex bend. Once a reasonable set of linear lattice solutions is established, we switch some of the drift bins to chromatic sextupoles for chromaticity correction, to harmonic sextupoles or octupoles for optimization of dynamic aperture and momentum aperture, and to correctors and BPMs for orbit correction.

In addition, the P constraints of Δs and Δp in Eq. (1) include: (i) The bending angles of each half central CB and outer CB are chosen as 4° and 2°, respectively. (ii) The bending field is below 0.5 T (i.e., bending angle of each PMQ is below 15 mrad, when length is 30 cm and beam energy is 3 GeV), and the gradient value is below 130 T/m as imposed by the field limitations at the chosen PMQ bore radius of 8 mm.

At this point, the P space is defined. It is worth noting here that the bins could be redefined during the optimization process. For instance, one might want to increase an ID straight length or need to slightly adjust the lattice to match

0.1	0.2	0.3	0.4	0.5	0.6
0.7	0.8	0.9	1	1.1	1.2
1.3	1.4	1.5	1.6	1.7	1.8
1.9	2	2.1	2.2	2.3	2.4
2.5	2.6	2.7	2.8	2.9	3
3.1	3.2	3.3	3.4	3.5	3.6
3.7	3.8	3.9	4	4.1	4.2
4.3	4.35 4.4	4.5	4.6	4.7	4.75 4.8
4.9	5	5.1	5.15 5.2	5.3	5.4
5.5	5.6	5.7	5.8	5.9	6
6.1	6.2	6.3	6.4	6.5	6.6
6.7	6.8	6.9	7	7.1	7.2
7.3	7.35 7.4	7.5	7.55 7.6	7.65 7.7	7.75 7.8
7.9	8	8.1	8.2	8.3	8.4
8.5	8.6	8.7	8.75 8.8	8.9	8.95 9
9.1	9.2	9.3	9.4	9.5	9.6
9.7	9.8	9.9	10	10.1	10.2
10.3	10.4	10.5	10.6	10.7	10.8
10.9	11	11.1	11.2	11.3	11.4
11.5	11.6	11.7	11.8	11.9	12
12.1	12.2	12.3	12.4	12.5	12.6
12.7	12.8	12.9	13	13.1	13.2
13.3	13.4	13.5	13.6	13.65 13.7	13.8
13.9	14 14.05	14.1	14.2	14.3	14.4
14.5	14.6	14.7	14.8	14.9	15
15.1	15.2	15.3	15.4	15.5	15.6
15.7	15.8	15.9	16	16.1	16.2
16.3	16.4	16.5	16.6	16.7	16.8
16.9	17	17.1	17.2	17.3	17.4
17.5	17.6	17.7	17.8	17.9	18
18.1	18.2	18.3	18.4	18.5	18.6
18.65 18.7	18.8	18.85 18.9	19	19.1	19.2
19.3	19.4	19.5	19.6	19.7	19.8
19.85 19.9	20 20.05	20.1 20.15	20.2	20.25 20.3	20.4
20.5	20.6	20.7	20.8	20.9	21
21.1	21.2	21.3	21.4	21.5	21.6
21.7	21.8	21.9	22	22.1	22.2
22.3	22.4	22.45 22.5	22.6	22.7	22.75 22.8
22.9	23	23.1	23.2	23.3	23.35 23.4
23.5	23.6	23.7	23.8	23.9	24
24.1	24.2	24.3	24.4	24.5	24.6
24.7	24.8	24.9	25	25.1	25.2
25.3	25.4	25.5	25.6	25.7	25.8
25.9	26	26.1	26.2	26.3	26.4

	K_0	K_1	K_2	K_3	Type
	0	0	0	0	Drift
	1	1	0	0	CB
	0	1	0	0	Quadrupole
	0	0	1	0	Sextupole
	0	0	0	1	Octupole

FIG. 3. Arrangement of bins for a single cell, where adjacent bins of the same type are grouped into an element. The type of element is marked with a specific color. The two outer CBs are located within the ranges of 5.8 to 7.2 m and 20.5 to 21.9 m. The central CB is located at 10.6 to 17.1 m with a 30-cm gap for a 3PW in the middle. The dispersion bumps are the sections between the central CB and the two outer CBs.

with the NSLS-II floor coordinates. It is relatively easy to accomplish, as sliding the bins in either direction and changing their properties is realized in a 1D vector describing the whole cell. Furthermore, this technique makes it seamless to develop special cells, such as injection or double minimum beta cells, as just a few bins are reoptimized. Finally, if we need a lower emittance lattice, it is straightforward to change several bins from drifts to CB PMQs and rerun the optimization loop.

B. Setup of the functional form $\mathcal{M}$

In the next step, a single cell is broken into sections of the bin areas as shown in Fig. 4, which correspond to the layout table presented in Fig. 3. The LS, OCB, DB, CCB, 3PW, QFC, and SS stand for long straight, outer complex bend, dispersion bump, central complex bend, three-pole wiggler, central quadrupole, and short straight. Each section is optimized separately in the following order: central complex bend, dispersion bump, outer complex bend, and straight sections. The matching conditions (constraints on the Twiss parameters) related to the $\mathcal{M}$ constraints of $\Delta\mathcal{M}$ in Eq. (1) need to be satisfied when interfacing these sections: (i) The mirror condition $(\alpha_x, \alpha_y, \eta_x') = 0$ should be matched in the center of CCB, and $(\beta_x, \beta_y, \eta_x)$ could be determined subject to further optimization. (ii) In the center of DB, a large dispersion height η_x is desired. In addition, optimal η_x' and α_y are set to create a dispersion region for placing sextupoles. (iii) The phase advance between two DBs should be matched close to $(3\pi, \pi)$ so that the $-\mathcal{I}$ transformation between a pair of chromatic sextupoles will help to cancel third-order geometrical RDTs within a cell. (iv) At the end of OCB, the η_x and η_x' are matched to zero for dispersion-free straight sections. (v) In the center of straights/IDs, the Twiss functions (β_x, β_y) are matched to less than 3 m for higher brightness of the photon beam with $(\alpha_x, \alpha_y) = 0$ for creating the beam waists. (vi) The overall beta functions do not exceed 25 m to keep chromaticities within a reasonable range. (vii) Length of each section is fixed as defined by the geometry of the tunnel.

C. Setup of the O space

Next, we discuss the process of setting up the O space. The observables of O space include: C_1: natural emittance ϵ_{x0}; C_2: natural chromaticities $\boldsymbol{\xi}$; C_3: radiation loss per turn U_0; C_4: momentum compaction α_c; and C_5: lengths of long and short straights $\boldsymbol{L_s}$.

These figures of merit define the O space. The selection of the best solution is in finding a lattice yielding the best function $\mathcal{F}$, which is defined as a weighted sum of observables in the O space:

$$\mathcal{F} = \sum_i \omega_i C_i, \tag{2}$$

where C_i represents each observable and ω_i indicates the corresponding weight. To achieve minimal value of function $\mathcal{F}$ in lattice design, $1/\alpha_c$ and $1/\boldsymbol{L_s}$ are used, as larger α_c and $\boldsymbol{L_s}$ are desired.

We have chosen the O constraints of ΔO in Eq. (1) as follows: (i) Horizontal partition number J_x within the range of [1.8, 2.3]; (ii) momentum compaction $\alpha_c > 5 \times 10^{-5}$; and (iii) minimum lengths $\boldsymbol{L_s}$ of long straight and short straight are 8.4 and 5.4 m, respectively.

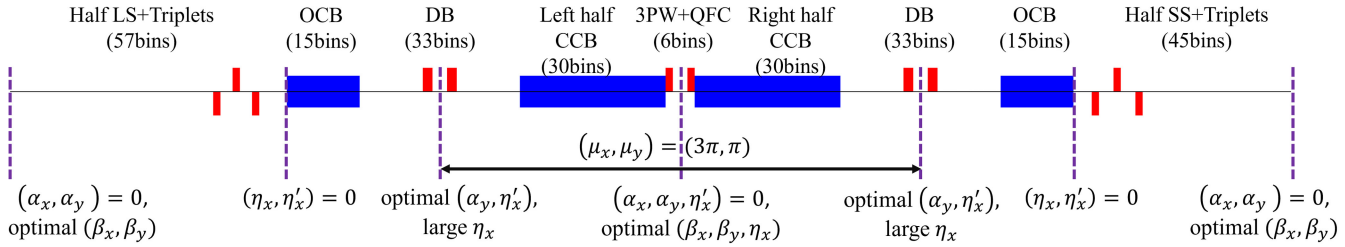

FIG. 4. Sections of a single cell with their corresponding number of bins, where red and blue blocks represent quadrupoles and complex bends, respectively. Labels in the bottom line indicate the $\mathcal{M}$ constraints of $\Delta\mathcal{M}$ in the center of long straight, at the end of outer complex bend, in the center of dispersion bump, in the center of central complex bend, and in the center of short straight.

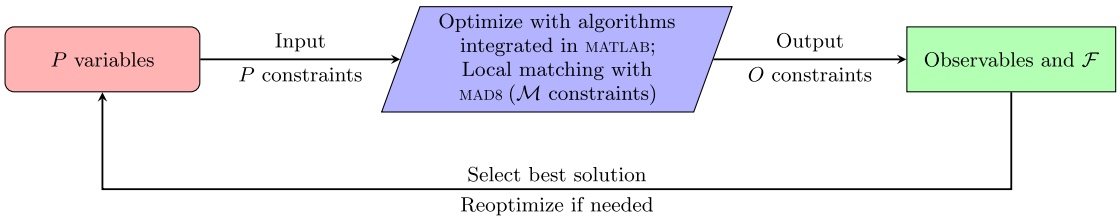

FIG. 5. Flowchart of optimization process.

D. Setup of the optimization method

Figure 5 illustrates the optimization process for solving Eq. (1) [23]. The NSGA-II algorithm [29] integrated into the MATLAB scripts [30] has been employed with an interface to the MAD8 program [27] for carrying out the local matching. Local matching is realized in MAD8 under constraints given by initial and final Twiss parameters. In NSGA-II, the chromosome is a vector of P variables, and the gene is a variable. The altered P variables (gradient values) are then carried over to the chromosome to generate a new population. Under the O constraints, the optimized solutions output the observables, and the corresponding function $\mathcal{F}$ is calculated. The best solution will be selected if the outputs reach the target values, otherwise, the next round of optimization will be conducted. For the setup of the NSGA-II algorithm, the simulated binary crossover and polynomial mutation are used with the distribution indices for crossover and mutation equal to 20. The crossover probability is set to 0.9, and mutation probability is chosen as $1/n$, where n is the number of decision variables. To evenly sample the points in the decision space, the Latin hypercube sampling [31] method is used to generate the initial population. The population size in each generation is set to 2000.

III. DESIGN OF CBA LATTICE

A. Central complex bend and dispersion bump optimization

Figure 6 displays the layout of right half CCB and half dispersion bump. The source planned for a 3PW beamline is in the drift space of CCB, and the center quadrupole is used to match mirror conditions. In the dispersion bump section, two symmetrical QFs are separated by a drift space for placing a sextupole.

To optimize the right half CCB, the field distributions of PMQs are flexibly defined to follow an analytical function with a total bending angle of 4°. For example, all PMQs follow a polynomial or piece-wise function. In our work, the CCB1 (PMQ1 to PMQ5) and CCB2 (PMQ6 to PMQ10) are optimized separately and $K_{0,i}$ and $K_{1,i}$ of PMQ1 to PMQ10 are defined as the following distributions:

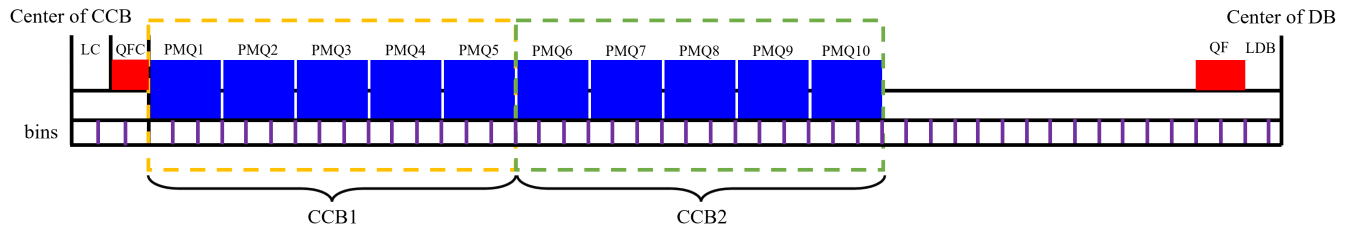

FIG. 6. Illustration of layout of right half CCB containing 10 PMQs and half dispersion bump. LC is the half drift length of the reserved space for a 3PW. QFC is the center quadrupole that matches mirror conditions in the center of CCB. QF is the quadrupole placed in the dispersion bump, and LDB is the half drift length between two QFs.

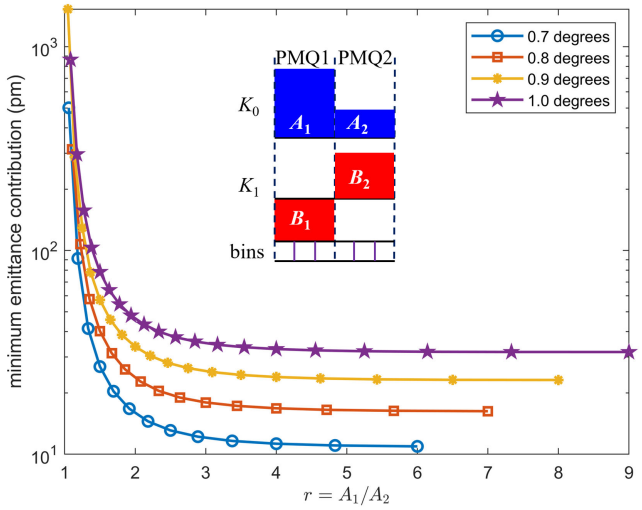

FIG. 7. Scan results for FODO-like PMQs (PMQ1 and PMQ2) with four different A_{sum} ($= A_1 + A_2$) range from 0.7° to 1.0° with an interval of 0.1°. The plot displays the minimum emittance contribution from FODO-like PMQs versus the ratios of r ($= A_1/A_2$). The inner picture indicates that PMQ with a large bending angle should be defocusing.

$$K_{0,i} = \begin{cases} A_1, & i = 1, 3, 5 \\ A_2, & i = 2, 4 \\ \sum_m a_m (i-6)^m, & i = 6, \ldots, 10, m = 0, \ldots, 3, \end{cases} \tag{3}$$

$$K_{1,i} = \begin{cases} B_1, & i = 1, 3, 5 \\ B_2, & i = 2, 4 \\ \text{optimal } K_{1,i}, & i = 6, \ldots, 10, \end{cases} \tag{4}$$

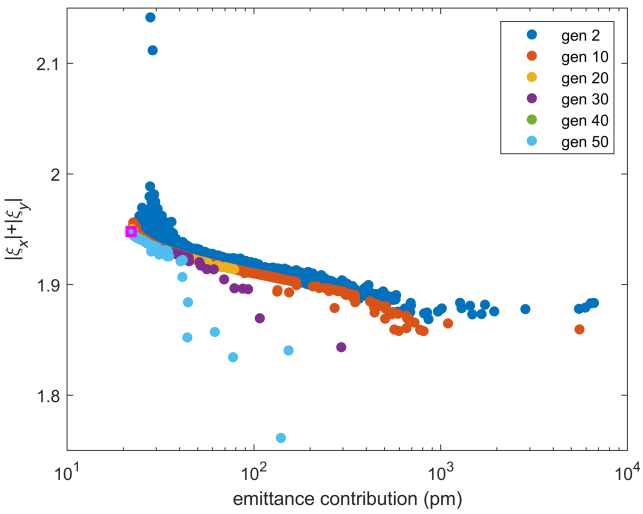

FIG. 8. Evolution of distributions of objective values in generations 2, 10, 20, 30, 40, and 50, where different colors represent different generations, and the selected solution is marked with a magenta box.

where i is the index of PMQ and a_m are the coefficients of a polynomial function. In addition, A_1, A_2, B_1, and B_2 are the coefficients of step-wise periodic functions. The conversion of optimization variables to the coefficients of functions reduces the number of P variables by a number of 5, which significantly benefits the search for optimal solutions in a complicated decision space.

The optimal A_1, A_2, B_1, and B_2 for CCB1 are found by scanning FODO-like PMQs (PMQ1 and PMQ2) with the objective of minimizing quantum excitation, which is approximately proportional to the emittance contribution. Figure 7 shows the scan results for different A_{sum} with varied r, where r is the ratio of A_1 to A_2 and A_{sum} is the sum of A_1 and A_2. With the considerations of emittance contribution and allocation of bending angles for CCB1 and CCB2, we choose $A_1 = 0.6°$ and $A_2 = 0.2°$ with their corresponding gradient values are $B_1 = -11\ \text{m}^{-2}$ and $B_2 = 13\ \text{m}^{-2}$, respectively.

We optimize CCB2 and half DB simultaneously using the method described in Sec. II D. The optimization variables include a_m, $K_{1,i}$ of CCB2, K_1 of QF, and drift length LDB. The optimization objectives are evaluated from the center of CCB to the center of DB, as shown in Fig. 6. The optimization goal is to simultaneously minimize emittance contribution from right half CCB and the sum of absolute natural chromaticities $|\xi_x| + |\xi_y|$. Figure 8 presents the evolution of distributions of objective values in generations 2, 10, 20, 30, 40, and 50. The optimization is almost converged after 50 generations. The selected solution is marked with a magenta box with a value of about 22 pm for emittance contribution.

Figure 9 presents the field values and corresponding Twiss function values for the selected solution, where the

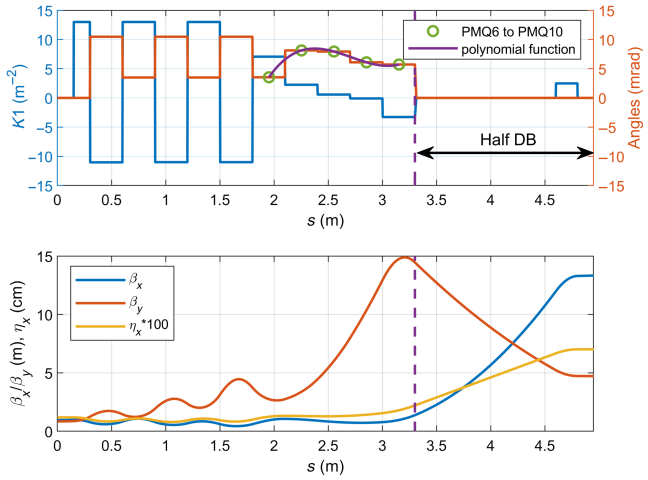

FIG. 9. Top plot: field values from the center of CCB to the center of DB, including the values of field gradients and bending angles, where green circles show the selected bending angles of CCB2 (PMQ6 to PMQ10) follow a polynomial function. Bottom plot: the corresponding Twiss function values from the center of CCB to the center of DB.

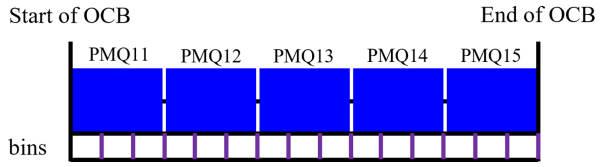

FIG. 10. Illustration of layout of OCB containing PMQ11 to PMQ15.

purple dashed line indicates the end of right half CCB and the start of the dispersion bump. A short 3PW is planned to be installed in the gap of CCB for the source of a beamline and aligned to the window in the rachet wall [32]. In the top plot, the optimized bending angles of CCB2 are represented by the green circles, which show they follow a polynomial function. The bottom plot shows Twiss function values from the center of CCB to the center of DB, and the phase advance is matched close to $(1.5\pi, 0.5\pi)$. Therefore, when introducing three sextupole families (one for focusing and two for defocusing) in the two dispersion bumps, the symmetrical beta functions (β_x, β_y) and the phase advance of $(3\pi, \pi)$ between three pairs of sextupoles will enable effective cancellation of third-order geometrical resonance driving terms (RDTs) [33] within a cell.

B. Outer complex bend optimization

Figure 10 illustrates the layout of OCB containing PMQ11 to PMQ15. Similar as we did in CCB2 optimization, the variables of a_m and $K_{1,i}$ of OCB are optimized under the constraint of a 2° total bending angle. The optimization objectives are evaluated from the center of CCB to the end of OCB, containing both CCB and OCB segments, even though only OCB is optimized. The goal of optimization is to simultaneously minimize emittance and the sum of absolute natural chromaticities $|\xi_x| + |\xi_y|$. In reality, we calculate the emittance for the entire ring by evaluating the contributions from each CB segment within it. Because the optical functions for CB segments are symmetrical, the emittance presented here accurately reflects the actual emittance of the storage ring.

Figure 11 shows the optimization results with two rounds using the method described in Sec. II D. The second round can start from the first round due to the stochastic characters of the NSGA-II algorithm. As shown in Fig. 11, the optimization almost converges after 34 generations in the second round. It is clear to note the "chromaticity wall" when pushing emittance close to 22 pm. This shape of distributions of objective values indicates that a solution with lower chromaticities can be selected without sacrificing emittance too much. However, in the selection of a solution, the Twiss function values at the end of OCB need to be considered for subsequent matching of straight sections. Consequently, the selected solution is marked with a magenta box in Fig. 11, which indicates that the ring's natural emittance is about 23 pm.

The top plot of Fig. 12 shows the values of magnetic fields and field gradients for the selected solution for the outer complex bend, where the green circles represent

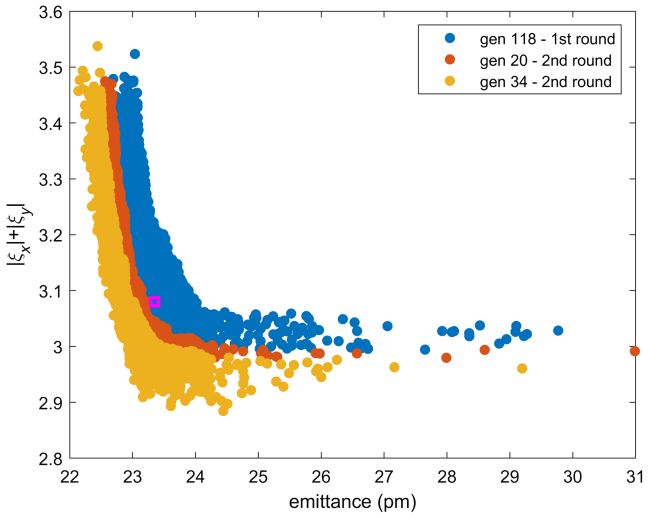

FIG. 11. Evolution of distributions of objective values in generation 118 of the first round and in generations 20 and 34 of the second round, where different colors represent different generations, and the selected solution is marked with a magenta box.

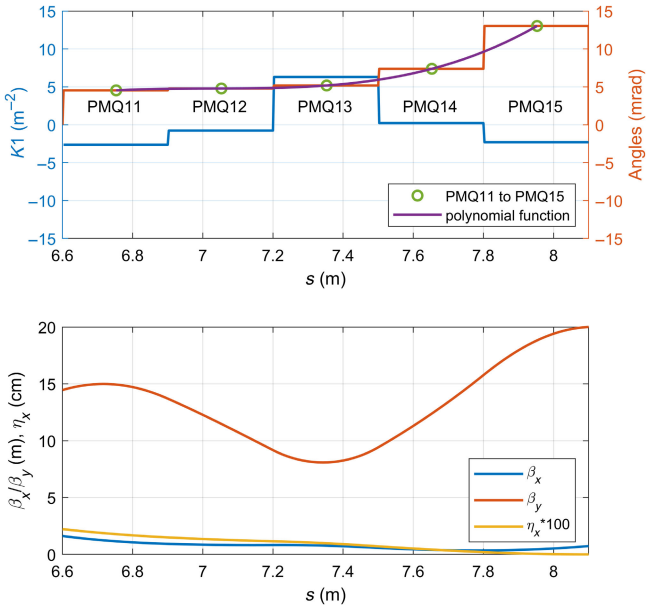

FIG. 12. Top plot: field values from the start of OCB to the end of OCB including the values of field gradients and bending angles, where green circles show the selected bending angles of PMQ11 to PMQ15 follow a polynomial function. Bottom plot: the corresponding Twiss function values from the start of OCB to the end of OCB.

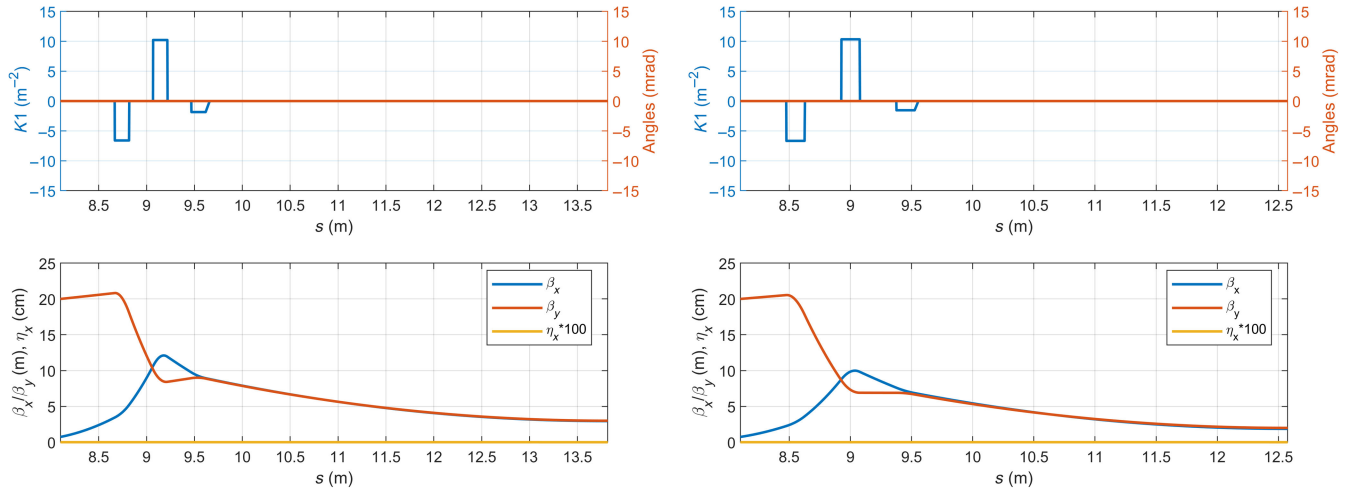

FIG. 13. Field gradients and positions of matching triplets, along with corresponding Twiss function values for half of the long straight section (left plot) and half of the short straight section (right plot) within a standard cell.

bending angles of PMQ11 to PMQ15. The bottom plot of Fig. 12 presents the Twiss function values along the outer complex bend.

C. Straight section design

After referring to the layout of the NSLS-II straight sections used to place diagnostic instrumentation, vacuum components, rf cavities, etc., the O constraints on the minimum lengths required for the entire long straight and short straight should be 8.4 and 5.4 m, respectively. Taking the Twiss function values at the end of OCB as the initial conditions, the positions and strengths of matching triplets are optimized to match the Twiss functions in the center of straights/IDs. The optimized field gradients and positions of matching triplets, along with corresponding Twiss function values for half of the long straight section and half of the short straight section, are displayed in the left and right plots of Fig. 13, respectively. As indicated by Fig. 13, the achieved lengths for half of the long straight and half of the short straight are 4.2 and 3.05 m, respectively.

D. Complex bend achromat lattice solution

As a result of the optimization described above, we continue with the lattice design by integrating the following sections: central complex bend, dispersion bumps, outer complex bends, and straight sections. The top plot of Fig. 14 shows the layout of magnets and Twiss function values along one standard supercell, starting from the center of a single short straight section to the center of the next short straight section. Due to the compact arrangement of complex bend elements, a substantial amount of free space (∼50%) is available for various accelerator equipment, including correctors, vacuum components, and diagnostic devices, etc. Furthermore, due to our choice of permanent magnet technology, the number of power supplies will be largely reduced, and the power consumption regarding magnets will be roughly 20% of that for the NSLS-II lattice.

The parameters and their values for the developed complex bend lattice at 3 GeV composed from 15 standard supercells are listed in Table I compared to the NSLS-II bare lattice. The natural emittance of the NSLS-II upgrade lattice is minimized to approximately 23 pm at 3 GeV, which is about 90 times smaller than that of the NSLS-II bare lattice. The beta functions in the center of the long straight are between 2 and 3 m, and they are between 1 and 2 m in the center of the short straight. In addition, the ID source points of developed NSLS-IIU lattice match with the NSLS-II lattice layout within 100 μm. These benefits for user programs demonstrate the advantages of employing complex bend lattice for NSLS-II upgrade.

The middle plot of Fig. 14 shows the Twiss function values along one supercell with double minimum beta functions in the long straight section, which are created by putting a triplets in the middle of the long straight section as denoted by the purple ellipse.

In practice, the NSLS-II upgrade lattice may consist of one supercell with high beta functions shown in the bottom plot of Fig. 14 for off-axis injection, and the rest are standard supercells for IDs. Double minimum beta structures will possibly replace several supercells.

Table II shows a comparison of multibend lattices for several facilities with the complex bend lattice for NSLS-IIU. The NSLS-IIU CBA lattice features a long straight for every supercell, offering the opportunity for the installation of long or tandem/canted undulators to provide higher photon beam energy and brightness. In the future, new alignment and correction techniques may be necessary to adapt to this novel lattice structure.

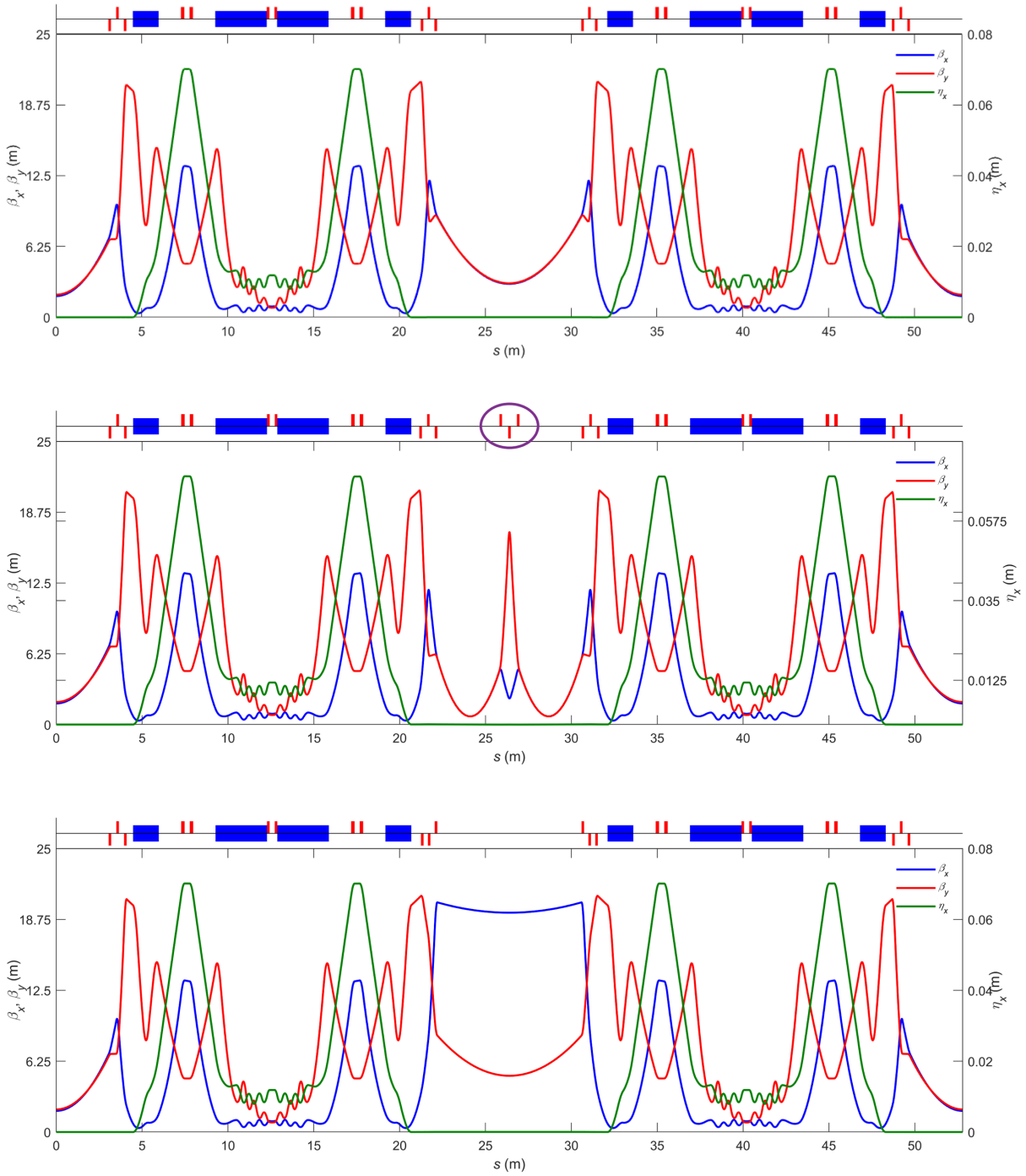

FIG. 14. Layout of magnets and Twiss function values along one supercell for standard structure, double minimum beta structure, and high beta structure from the top to the bottom plots, starting from the center of a single short straight to the center of the next short straight. The complex bends are colored blue, and the red blocks represent the quadrupoles. The sextupoles and octupoles are not shown in this figure.

E. Nonlinear dynamics optimization

The nonlinear dynamics optimization targeting sufficient dynamic and momentum apertures is in progress at the time of writing this paper, so we are presenting here some preliminary results. We installed three chromatic sextupole families used to correct the chromaticities (ξ_x, ξ_y) to $(+2, +2)$ as shown in Fig. 15. The phase advances between three pairs of sextupoles are close to $(3\pi, \pi)$ to cancel the third-order geometrical resonance driving terms (RDTs). To further improve the performance of DA and MA, three chromatic octupole families are also placed in phase with three chromatic sextupole families to simultaneously

TABLE I. Parameters of the NSLS-II bare lattice and the developed NSLS-IIU CBA lattice comprise 15 standard supercells operating at 3 GeV.

Paramters	Values	
	NSLS-II bare lattice	NSLS-IIU CBA lattice
Circumference C (m)	791.958	791.7679
Beam energy E (GeV)	3	3
Natural emittance ϵ_{x0} (pm-rad)	2086	23.4
Damping partitions (J_x, J_y, J_δ)	(1, 1, 2)	(2.24, 1, 0.76)
Ring tunes (ν_x, ν_y)	(33.22, 16.26)	(84.67, 28.87)
Natural chromaticities (ξ_x, ξ_y)	(−98.5, −40.2)	(−135, −144)
Momentum compaction α_c	3.63×10^{-4}	7.76×10^{-5}
Energy loss per turn U_0 (keV)	286.4	196
Energy spread σ_δ (%)	0.0514	0.073
(β_x, β_y) at LS center (m)	(20.1, 3.4)	(2.95, 2.99)
(β_x, β_y) at SS center (m)	(1.8, 1.1)	(1.87, 1.99)
($\beta_{x,\max}$, $\beta_{y,\max}$) (m)	(29.99, 27.31)	(13.37, 20.82)
($\beta_{x,\min}$, $\beta_{y,\min}$) (m)	(1.84, 1.17)	(0.35, 0.84)
($\beta_{x,\text{avg}}$, $\beta_{y,\text{avg}}$) (m)	(12.58, 13.79)	(3.99, 7.51)
Length of long straight L_{LS} (m)	9.3	8.4
Length of short straight L_{SS} (m)	6.6	6.1
Sum of K_2 of chromatic sextupoles per cell (m^{-3})	∼100	∼1600
rms bunch length at $V_{\text{rf}} = 3$ MV and $f_{\text{rf}} = 499.681$ MHz (mm)	2.70	1.77

TABLE II. Comparison of multibend lattices from several facilities with respect to the complex bend lattice for NSLS-IIU.

	C (m)	E (GeV)	ϵ_{x0} (pm-rad)	$\boldsymbol{L_s}$ (m)	α_c ($\times 10^{-5}$)	σ_δ (%)	U_0 (MeV)
NSLS-IIU CBA	791.7679	3	23	(8.4, 6.1)	7.76	0.073	0.196
ALS-U [8]	196.51	2	108	∼5	20.3	0.102	0.245
SLS-II [14]	288	2.7	158	∼(12, 6, 4)	10.5	0.116	0.688
SOLEIL II [10,11]	353.97	2.75	83	(3.1, 3.7, 4.2, 7.9, 9.0)	10.6	0.091	0.453
SIRIUS [4,34]	518.4	3	250	(7.5, 6.5)	16.3	0.085	0.475
KOREA-4GSR [12]	799	4	58	6.5	7.86	0.120	1.010
ESRF-EBS [5]	843.98	6	133	5.3	8.51	0.094	2.56
APS-U [6]	1103.61	6	42	∼6	4.04	0.135	2.870
HEPS [9]	1360.4	6	34	∼6	1.56	0.106	2.890

correct the fourth-order geometrical resonance driving terms (RDTs) and amplitude-dependent tune shift (ADTs) [35]. Particle tracking simulations are carried out with the elegant [36].

During the early stage of nonlinear dynamics optimization, we assume that the CB lattice consists of 30 cells, with one long straight section matched to achieve high beta at the injection point (see the bottom plot of Fig. 14). The ring

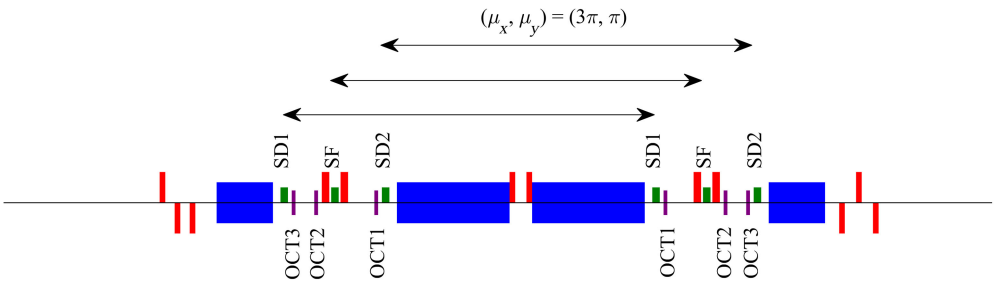

FIG. 15. Locations of three chromatic sextupole families and three chromatic octupole families in the high beta cell. The phase advances between three pairs of sextupoles are close to $(3\pi, \pi)$.

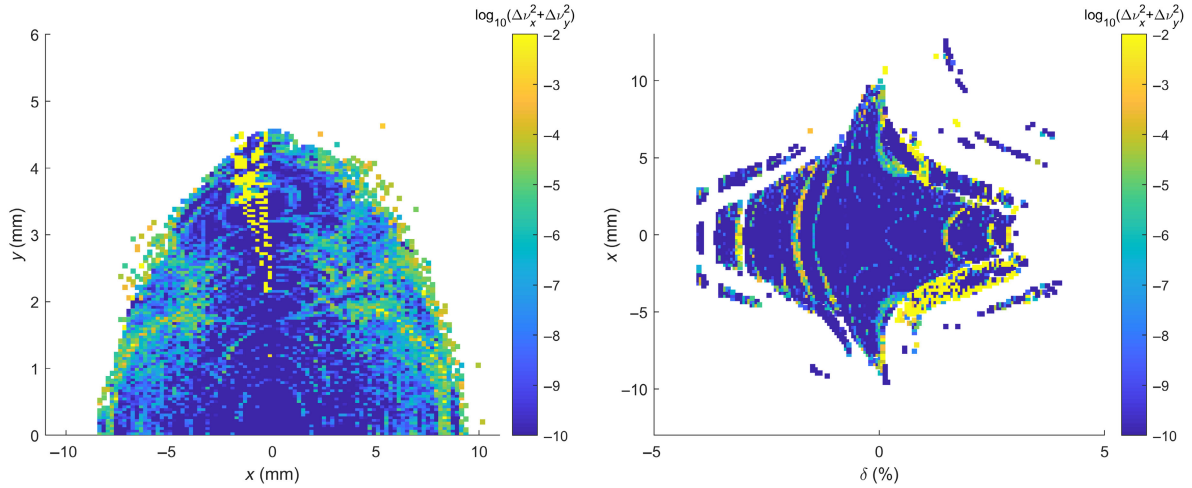

FIG. 16. On-momentum frequency map (left) and off-momentum frequency map (right) at the injection point. The maps are generated by tracking particles for 1024 turns.

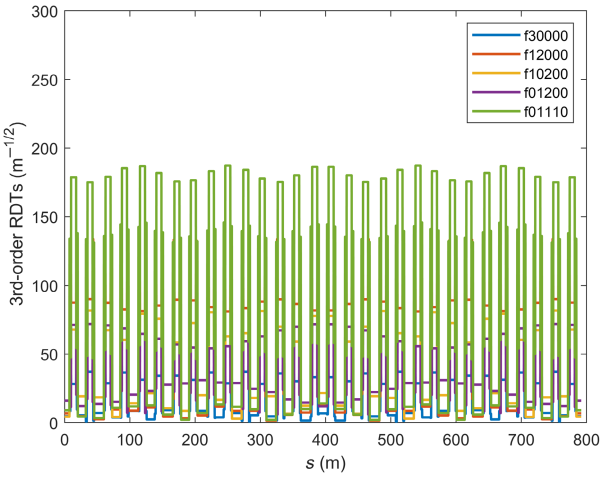

FIG. 17. Amplitude variation of third-order RDTs along the whole complex bend achromat ring lattice.

tunes are moved to $(\nu_x, \nu_y) = (84.219, 28.273)$ to away from leading order resonances. To further enlarge the DA and MA, the positions and strengths of chromatic sextupoles and chromatic octupoles are optimized. One of our recent optimized results for on-momentum and off-momentum frequency maps is shown in Fig. 16. At the injection point, the achieved range of DA is approximately $-9/+9$ mm, and MA has reached about 3%. The amplitude of third-order RDTs along the whole ring for this nonlinear solution is also displayed in Fig. 17. In the future, methods of using harmonic sextupoles [37], minimizing the fluctuation of RDTs [38], and optimizing the W functions [39] can be used to maximize the dynamic aperture and momentum aperture.

One goal of the storage ring lattice design is to deliver a robust lattice resilient to errors and imperfections. To check the robustness of a lattice, it typically generates

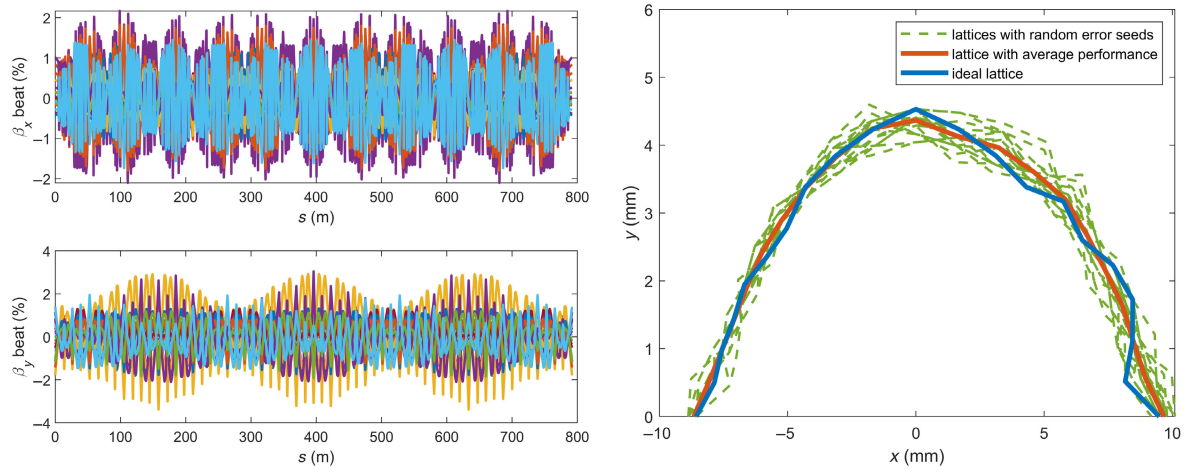

FIG. 18. β-beat of 20 perturbed lattices with random error seeds (left). On-momentum dynamic aperture of ideal lattice, lattices with random error seeds, and lattice with average performance (right).

several perturbed lattices, each having a random error seed, and then evaluates their performances. In our work, we generated 20 lattices with random gradient errors. No alignment errors are specified, as they will be addressed in future detailed studies. The level of gradient errors to complex bends and quadrupoles is chosen to have an amplitude of 0.02% (rms) to cause a beta-beating on the order of 1%–2% in both horizontal and vertical planes, as shown in the left plot of Fig. 18. It simulates the residual beta-beating after the lattice correction in the real machine. In addition, the random errors introduced to sextupoles and octupoles have an amplitude of 0.01% (rms). The right plot in Fig. 18 presents the on-momentum dynamic aperture tracking results for 20 perturbed lattices. The average performance of the perturbed lattices is close to the ideal lattice.

IV. CONCLUSIONS

We presented the complex bend (CB) approach in the lattice design exemplified for the case of the NSLS-II upgrade lattice.

The advantages of using the CB approach for the high-performance lattice design are demonstrated as follows: (i) We achieved a low natural emittance of 23 pm and a path of further reducing the emittance by adding more CB poles to the elements in the lattice will be demonstrated in the future work. (ii) The 8.4-m-long long straight and 6.1-m-long short straight provide room for long IDs and hence help to achieve higher brightness of photon beam. (iii) A larger free space in the lattice is available for accelerator equipment, where the fraction of free space to the ring circumference is about 50%. This larger free space, if not fully used by accelerator equipment, could be used for additional CB poles, thus potentially further improving the performances of the lattice in terms of natural horizontal emittance. (iv) The use of complex bend reduces the number of power supplies, and overall power consumption by the magnet system for the developed NSLS-II upgrade lattice is about 20% of that for the present NSLS-II lattice. (v) On-going nonlinear dynamics optimization has already indicated appreciable DA and MA. The work is continuing in an effort to secure efficient injection and long beam lifetime.

Thus far, the hard-edge model for the complex bend is being used, and more accurate magnet modeling is needed.

ACKNOWLEDGMENTS

We are grateful for discussions and advice from our collaborators in planning the NSLS-II upgrade Yongjun Li, Yoshiteru Hidaka, Victor Smalyuk, Guimei Wang, Sushil Sharma, Bernard Kosciuk, Jinhyuk Choi, Aamna Khan, Gabriele Bassi, and Xi Yang. We express sincere appreciation to Simon White from ESRF for proofreading the manuscript and giving us valuable feedback. This work has been supported by United States DOE under Contract No. DE-SC0012704 and Brookhaven National Laboratory Directed Research and Development Program, Project No. 20-041 "Conceptual Design Options for Future Upgrade of NSLS-II Facility."

APPENDIX A: ESTIMATION OF RADIATION INTEGRALS WITH BINS

The natural emittance, radiation loss, and momentum compaction of a CBA lattice have the following relations with radiation integrals [1]:

$$\epsilon_{x0} \propto \frac{I_5}{I_2 - I_4}, \qquad U_0 \propto I_2, \qquad \alpha_c \propto I_1. \tag{A1}$$

The evaluations of radiation integrals contributed from short PMQs of complex bends are expressed as [40]

$$I_1 = \oint \eta_x h ds \approx \sum_i \langle \eta_x \rangle_i K_{0,i}, \tag{A2}$$

$$I_2 = \oint h^2 ds \approx \frac{1}{L} \sum_i K_{0,i}^2, \tag{A3}$$

$$I_3 = \oint |h|^3 ds \approx \frac{1}{L^2} \sum_i |K_{0,i}|^3, \tag{A4}$$

$$I_4 = \oint \eta_x (h^3 + 2hK_1) ds \approx \sum_i \left(\frac{K_{0,i}^3}{L^2} + 2K_{0,i} K_{1,i} \right) \langle \eta_x \rangle_i, \tag{A5}$$

$$I_5 = \oint |h|^3 \mathcal{H} ds \approx \frac{1}{L^2} \sum_i |K_{0,i}|^3 \langle \mathcal{H} \rangle_i, \tag{A6}$$

where $h = \frac{1}{\rho}$ is the orbit curvature, $\mathcal{H} = \gamma_x \eta_x^2 + 2\alpha_x \eta_x \eta_x' + \beta_x \eta_x'^2$ is the Courant-Snyder invariant defined by Twiss parameters (α_x, β_x, γ_x) and dispersion functions (η_x, η_x'). By taking advantage of the binning method mentioned in Sec. II, we can estimate radiation integrals via summations through the complex bend segments before further dividing the magnets into more slices to achieve more accurate results, where $K_{0,i}$ and $K_{1,i}$ are the bending angle and gradient value for ith PMQ with a constant length of $L = 3$ bins. In these equations, $\langle \eta_x \rangle_i$ and $\langle \mathcal{H} \rangle_i$ correspond to η_x and $\mathcal{H}$ of ith PMQ averaged along the respective bins.

APPENDIX B: OPTIMIZATION RANGES OF VARIABLES

The optimization ranges of variables used in the lattice design are summarized in Table III.

TABLE III. Optimization ranges of variables.

Optimization variables	Locations[a]	Units	Ranges
PMQ K1	CCB and OCB	m^{-2}	[−13, 13]
Polynomial a_0	CCB	⋯	[0.1, 0.85]
Polynomial a_0	OCB	⋯	[0, 0.85]
Polynomial a_1	CCB and OCB	⋯	[−0.5, 0.5]
Polynomial a_3	CCB and OCB	⋯	[−0.1, 0.1]
Quadrupole	DB	m^{-2}	[−3, 3]
Quadrupole	QFC and Matching Triplets	m^{-2}	[−13, 13]
Sextupole	DB	m^{-3}	[−400, 400]
Octupole	DB	m^{-4}	[−100 000, 100 000]

[a]The full name of these locations can be found in Fig. 4.

[1] S.-Y. Lee, *Accelerator Physics* (World Scientific Publishing Company, Singapore, 2018).

[2] D. Einfeld, J. Schaper, and M. Plesko, Design of a diffraction limited light source (DIFL), in *Proceedings of the Particle Accelerator Conference, Dallas, TX* (IEEE, New York, 1995), Vol. 1, pp. 177–179.

[3] S. C. Leemann, M. Sjöström, and Å. Andersson, First optics and beam dynamics studies on the MAX IV 3 GeV storage ring, Nucl. Instrum. Methods Phys. Res., Sect. A **883**, 33 (2018).

[4] A. Rodrigues *et al.*, Sirius light source status report, in *Proceedings of the 9th International Particle Accelerator Conference, IPAC-2018, Vancouver, BC, Canada* (JACoW, Geneva, Switzerland, 2018), pp. 2886–2889, 10.18429/JACoW-IPAC2018-THXGBD4.

[5] P. Raimondi, N. Carmignani, L. R. Carver, J. Chavanne, L. Farvacque, G. Le Bec, D. Martin, S. M. Liuzzo, T. Perron, and S. White, Commissioning of the hybrid multibend achromat lattice at the European Synchrotron Radiation Facility, Phys. Rev. Accel. Beams **24**, 110701 (2021).

[6] T. E. Fornek, Advanced photon source upgrade project final design report, Report No. APSU-2.01-RPT-003, 2019, https://publications.anl.gov/anlpubs/2019/07/153666.pdf.

[7] C. Steier *et al.*, Completion of the brightness upgrade of the ALS, J. Phys. Conf. Ser. **493**, 012030 (2014).

[8] T. Hellert, C. Steier, and M. Venturini, Lattice correction and commissioning simulation of the Advanced Light Source upgrade storage ring, Phys. Rev. Accel. Beams **25**, 110701 (2022).

[9] Y. Jiao, G. Xu, X.-H. Cui, Z. Duan, Y.-Y. Guo, P. He, D.-H. Ji, J.-Y. Li, X.-Y. Li, C. Meng, Y.-M. Peng, S.-K. Tian, J.-Q. Wang, N. Wang, Y.-Y. Wei, H.-S. Xu, F. Yan, C.-H. Yu, Y.-L. Zhao, and Q. Qin, The HEPS project, The HEPS project, J. Synchrotron Radiat. **25**, 1611 (2018).

[10] A. Nadji and L. S. Nadolski on behalf of the SOLEIL II TDR Team, Upgrade project of the SOLEIL accelerator complex, Synchrotron Radiat. News **36**, 10 (2023).

[11] Conceptual Design Report: Synchrotron SOLEIL upgrade, 2021, https://www.synchrotron-soleil.fr/en/files/conceptual-design-report-synchrotron-soleil-upgrade.

[12] G. Jang, S. Shin, M. Yoon, J. Ko, Y. D. Yoon, J. Lee, and B.-H. Oh, Low emittance lattice design for Korea-4GSR, Nucl. Instrum. Methods Phys. Res., Sect. A **1034**, 166779 (2022).

[13] P. Raimondi and S. M. Liuzzo, Toward a diffraction limited light source, Phys. Rev. Accel. Beams **26**, 021601 (2023).

[14] A. Streun, M. Aiba, M. Böge, C. Calzolaio, M. Ehrlichman, M. Negrazus, B. Riemann, and V. Vrankovic, Swiss Light Source upgrade lattice design, Phys. Rev. Accel. Beams **26**, 091601 (2023).

[15] R. Bartolini *et al.*, Double-double bend achromat cell upgrade at the Diamond Light Source: From design to commissioning, Phys. Rev. Accel. Beams **21**, 050701 (2018).

[16] E. Karantzoulis, Elettra 2.0: The diffraction limited successor of Elettra, Nucl. Instrum. Methods Phys. Res., Sect. A **880**, 158 (2018).

[17] P. F. Tavares, J. Bengtsson, and Åke Andersson, Future development plans for the MAX IV light source: Pushing further towards higher brightness and coherence, J. Electron Spectrosc. Relat. Phenom. **224**, 8 (2018).

[18] T. Shaftan, V. Smaluk, and G. Wamg, Concept of the complex bend, Brookhaven National Lab, Upton, New York, Technical Report No. BNL-211211-2019-TECH, NSLSII-ASD-TN-276, 2018, https://technotes.bnl.gov/PDF?publicationId=211211.

[19] S. Sharma, Elements of engineering design of the upgrade lattice, BNL Retreat on Plans for NSLS-II Upgrade (2023).

[20] S. Brooks, Modified Halbach magnets for emerging accelerator applications, in *Proceedings of the 12th International Particle Accelerator Conference, IPAC-2021,*

Campinas, Brazil (JACoW, Geneva, Switzerland, 2021), pp. 1315–1318, 10.18429/JACoW-IPAC2021-TUXC07.

[21] P. N'gotta, G. Le Bec, and J. Chavanne, Hybrid high gradient permanent magnet quadrupole, Phys. Rev. Accel. Beams **19**, 122401 (2016).

[22] A. Ghaith, D. Oumbarek, C. Kitégi, M. Valléau, F. Marteau, and M.-E. Couprie, Permanent magnet-based quadrupoles for plasma acceleration sources, Instruments **3**, 27 (2019).

[23] T. Shaftan, Methodology for designing complex bend lattice, Brookhaven National Lab., Upton, New York, Technical Report No. BNL-223858-2023-TECH, NSLSII-ASD-TN-388, 2022, https://technotes.bnl.gov/PDF?publicationId=223858.

[24] G. Wang, T. Shaftan, V. Smaluk, N. A. Mezentsev, S. Sharma, O. Chubar, Y. Hidaka, and C. Spataro, Complex bend: Strong-focusing magnet for low-emittance synchrotrons, Phys. Rev. Accel. Beams **21**, 100703 (2018).

[25] G. Wang, T. Shaftan, V. Smaluk, Y. Hidaka, O. Chubar, T. Tanabe, J. Choi, S. Sharma, C. Spataro, and N. A. Mesentsev, Complex bend. II. A new optics solution, Phys. Rev. Accel. Beams **22**, 110703 (2019).

[26] G. Wang *et al.*, NSLS-II storage ring injection optimization, in *Proceedings of the 6th International Particle Accelerator Conference, IPAC-2015, Richmond, VA* (JACoW, Geneva, Switzerland, 2015), pp. 1968–1970, 10.18429/JACoW-IPAC2015-TUPHA004.

[27] H. Grote and F. C. Iselin, The MAD program (Methodical Accelerator Design), Version 8.13/8 user's reference manual, CERN, Technical Report No. CERN/SL/90-13 (AP) (Rev. 4), 1994, https://project-madwindows.web.cern.ch/MAD-resources/MAD8.13%20User%20Reference%20Manual.pdf.

[28] T. M. Inc., MATLAB version: 9.14.0.2306882 (R2023a), 2023.

[29] K. Deb, A. Pratap, S. Agarwal, and T. Meyarivan, A fast and elitist multiobjective genetic algorithm: NSGA-II, IEEE Trans. Evol. Comput. **6**, 182 (2002).

[30] A. Seshadri, NSGA-II: A multi-objective optimization algorithm, MATLAB Central File Exchange, 2020, https://www.mathworks.com/matlabcentral/fileexchange/10429-nsga-ii-a-multi-objective-optimization-algorithm.

[31] M. D. McKay, R. J. Beckman, and W. J. Conover, Comparison of three methods for selecting values of input variables in the analysis of output from a computer code, Technometrics **21**, 239 (1979).

[32] M. Breitfeller and S. Kramer, Innovative design of radiation shielding for synchrotron light sources, in *Proceedings of the 9th Edition of Mechanical Engineering Design of Synchrotron Radiation Equipment and Instrumentation Conference, MEDSI-2016, Barcelona, Spain* (JACoW, Geneva, Switzerland, 2017), pp. 321–323, 10.18429/JACoW-MEDSI2016-WEPE05.

[33] J. Bengtsson, The sextupole scheme for the Swiss Light Source (SLS): An analytic approach, SLS-Note **9**, 97 (1997).

[34] F. de Sá, L. Liu, and X. Resende, Optimization of nonlinear dynamics for sirius, in *Proceedings of the International Particle Accelerator Conference, IPAC-2016, Busan, Korea* (JACoW, Geneva, Switzerland, 2016), pp. 3409–3412, 10.18429/JACoW-IPAC2016-THPMR012.

[35] F. Plassard, G. Wang, T. Shaftan, V. Smaluk, Y. Li, and Y. Hidaka, Simultaneous correction of high order geometrical driving terms with octupoles in synchrotron light sources, Phys. Rev. Accel. Beams **24**, 114801 (2021).

[36] M. Borland, ELEGANT: A flexible SDDS-compliant code for accelerator simulation, in *Proceedings of the 6th International Computational Accelerator Physics Conference, ICAP 2000, Darmstadt, Germany* (2000), https://www.aps.anl.gov/files/APS-sync/lsnotes/files/APS_1418218.pdf.

[37] M. Song and Y. Li, Low emittance ring lattice design, BNL Retreat on Plans for NSLS-II Upgrade (2023).

[38] B. Wei, Z. Bai, J. Tan, L. Wang, and G. Feng, Minimizing the fluctuation of resonance driving terms in dynamic aperture optimization, Phys. Rev. Accel. Beams **26**, 084001 (2023).

[39] Y. Cai, Y. Nosochkov, J. S. Berg, J. Kewisch, Y. Li, D. Marx, C. Montag, S. Tepikian, F. Willeke, G. Hoffstaetter, and J. Unger, Optimization of chromatic optics in the electron storage ring of the Electron-Ion Collider, Phys. Rev. Accel. Beams **25**, 071001 (2022).

[40] R. H. Helm, M. J. Lee, P. Morton, and M. Sands, Evaluation of synchrotron radiation integrals, IEEE Trans. Nucl. Sci. **20**, 900 (1973).